Design and Optimization of High-Gain Bidirectional DC–DC Converter for Electric Vehicles

Yiliang Li, *Student Member, IEEE*, Yijie Wang, *Senior Member, IEEE*, Yueshi Guan, *Senior Member, IEEE*, and Dianguo Xu, *Fellow, IEEE*

***Abstract*—To better leverage and cope with the characteristics of low-voltage electric vehicle battery pack, this work optimizes the design of on-board bidirectional dc-dc converter. Based on the dual active half-bridge (DAHB) converter, combined with partial switch sharing, a high-gain bidirectional dc–dc converter is proposed. This converter has 48-V and 24-V output voltage levels, and the multiple voltage levels, which are often required by new energy vehicles, are able to reduce the number of on-board converters. The theoretical part of this work analyzes the design process of the converter, and in parallel, establishes the mathematical models of transmission power, soft switching, current stress, and reactive backflow loss. Under the condition of high gain, the system has good soft-switching characteristics and low reactive backflow loss. In the experimental part, a prototype with an input voltage of 400 V is built under an operating frequency of 100 kHz. The voltage of the two output ports is stable and a peak efficiency of 94.7% is achieved. The experimental results verify the validity of the theoretical analysis.**

***Index Terms*—Dual active half-bridge (DAHB), high-voltage gain, on-board charger, zero-voltage switching (ZVS).**

I. INTRODUCTION

WITH the aggravation of energy crisis and environmental pollution, societal demand for pollution-free electric vehicles (EVs) keeps increasing. Driven by policy mandates and technology advancements, intelligent EVs have experienced unprecedented development in recent years. With the increasing maturity of energy storage and power electronics technology, vehicle electrification and intelligence are trending. The diversity of on-board electronic devices on EVs has become an important part of intelligent transportation [1], [2]. The brief internal electrical architecture is shown in Fig. 1. With the increasing amount of electrical equipment, the onboard power system of EVs ought to have multiple voltage levels, including a 400-V high-voltage dc bus, so as to maintain the normal driving of EVs. The auxiliary power supply, which aims at providing the energy needed for power steering, air conditioning, electric windows, illumination, electronic display panel, among other electrical/electronic devices, is usually low-voltage dc at 12-, 24-, and 48-V [3], [4].

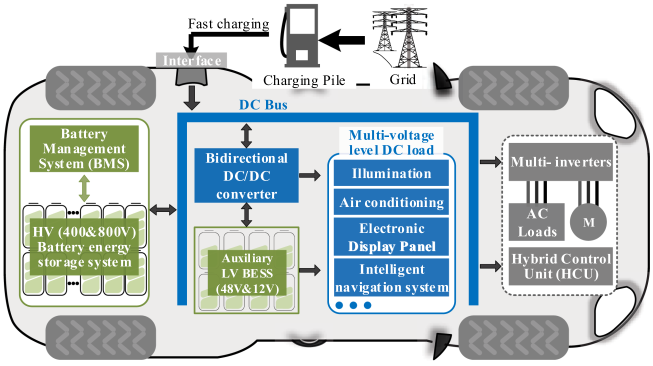

Fig. 1. Brief power system structure of EV.

To ensure the normal operation of EV and the onboard electrical equipment, and mitigate the voltage fluctuation problem, it is necessary to maintain the stability of the internal bus voltage, which can be realized through energy storage devices [5]. An interface of voltage conversion between low-voltage energy storage device and high-voltage dc bus still demands additionally. In this regard, the high-performance bidirectional dc–dc (BDC) converter provides such a link and is, thus, vital to control the bidirectional flow of energy and maintain the stability of dc bus [6], [7].

In energy storage systems (ESSs), BDC converters are required to operate with high gain and wide voltage range, due to the variable nature of battery charging state and the use of low-voltage and high-power-capacity battery charging technology. In addition, with the continuous development of automated and intelligent EVs, the on-board electrical equipment is diversified, hence, the BDC converters should be able to facilitate energy transfer between different voltage levels [8].

In nonisolated BDCs, optimized structures, such as coupled inductors or switched capacitors, are used to improve the voltage gain of the converter. However, the introduction of a large number of passive devices increases the model order and complexity. In addition, the inductor, capacitor, and switching frequency parameters of the circuit need to be strictly matched to avoid resonance interference [9], [10].

The isolated dc–dc converter achieves high voltage gain by adjusting the transformer turn ratio, with electrical isolation, which can operate at high voltage and power levels. However, the

---

Manuscript received 26 January 2023; revised 4 May 2023; accepted 3 June 2023. Date of publication 14 June 2023; date of current version 28 July 2023. This work was supported by National Natural Science Foundation of China under Grant 52007041. Recommended for publication by Associate Editor M. Hartmann. *(Corresponding author: Yijie Wang.)*

The authors are with the School of Electrical Engineering and Automation, Harbin Institute of Technology, Harbin 150001, China (e-mail: liylhit@qq.com; wangyijie@hit.edu.cn; hitguanyueshi@163.com; xudiang@hit.edu.cn).

Color versions of one or more figures in this article are available at https://doi.org/10.1109/TPEL.2023.3285627.

Digital Object Identifier 10.1109/TPEL.2023.3285627

TABLE I
SUMMARY OF EXISTING OPTIMIZATION METHODS

	Schemes	Advantages/Disadvantages
Control strategy	Extend ZVS range [15]	Full-load range ZVS/ Additional mode judgment.
	All loss optimization [17]	Highest efficiency / Off-line computing is necessary.
	Zero reactive loss [18]	Minimum reactive loss/ Operation is complicated.
Topology design	Device series parallel [20]	Simple topology /Inconsistency of component parameters
	Module series parallel [21]	Flexible voltage regulating ability / High hardware and control costs
	Additional resonance [23]	Wide ZVS range, low current stress/ Sensitive to parasitic parameters

high turn ratio reduces the coupling efficiency of the transformer, increases the parasitic leakage inductor and voltage stress. Additionally, the multiturn winding structure also leads to a significant increase in the weight and volume of the transformer. How to achieve high voltage gain under the condition of low turn ratio is a problem that power electronics engineers need to solve [11], [12].

With the advantages of bidirectional power processing, high power density and soft switching, dual active bridge (DAB), and dual active half-bridge (DAHB) have become a universal solution in electrical isolation occasions. However, under the high-gain condition, the large reactive loss and narrow soft-switching range limit the application of DAB and DAHB converters [13], [14]. Optimization from the perspective of control strategy and topology design can significantly improve the performance of the converter, and Table I briefly summarizes the existing optimization methods.

In terms of control strategies, the multidegree-of-control freedom methods are widely used, such as triple phase shift. By utilizing optimization methods, such as Lagrange multiplier method, the converter can obtain wide zero-voltage-switching (ZVS) range, low current stress, and reactive loss [15]. But the multiobjective optimization, especially under high-gain condition, requires complex mathematical modeling and extensive calculations. And the necessary offline computing results in limited portability [17], [18], [19].

In topology optimization, the series–parallel structure using multiple BDC as module is proposed to improve the voltage regulation capacity. Considering the inconsistent parameters of components and power modules, the characteristics of each module still have the risk of deterioration [21]. What is more, additional inductor–capacitor resonance introduced into the circuit to optimize the characteristics of the system [22]. The capacitor–inductor–inductor–capacitor (CLLC) structure has been widely used, shows advantages in soft switching, current stress. But resonant circuit is sensitive to parasitic parameters, and the asymmetric parasitic parameters affect the working state, which lead to the complexity and difficulty of parameter design, especially under high-gain conditions [24], [25].

In view of the existing research status quo, this work proposes an optimized topology of a bidirectional isolated converter for high-gain conditions. The proposed converter can enable efficient energy transfer between the dc-bus and low-voltage battery packs. Low reactive backflow losses reduce power electronics disturbances to bus voltage. In addition, the system has two output ports, which can supply power for dc loads and batteries of different voltage levels, saving the number of on-board converters in EVs.

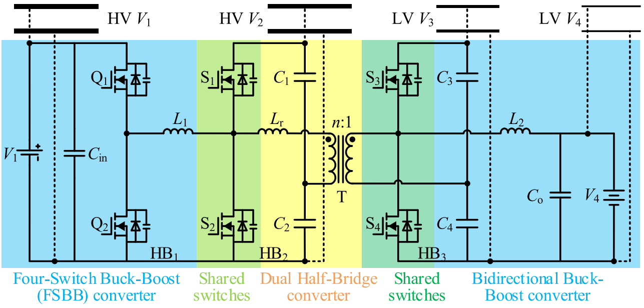

Fig. 2. Circuit topology of proposed HB^2-DAHB converter.

The rest of this work is organized as follows. In Section II, the circuit topology and operational principles are analyzed. Section III establishes the mathematical model of the soft-switching, current stress, and reactive backflow loss. An experimental prototype is built and tested to verify the validity of the theoretical analysis in Section IV. Finally, Section V concludes this article.

II. PROPOSED CONVERTER AND OPERATION PRINCIPLE

A. *Topology Description*

Compared to full-bridge structure, DAHB converter has less switches, especially with less cost in modular construction. The lower voltage stress of the transformer makes DAHB converters show advantages in high-voltage and high-gain applications. However, unlike DAB converter with multiple phase-shift angles, DAHB converter has only one interbridge phase-shift angle as a control degree. Poor control flexibility limits the optimization of converter performance. Considering DAHB converter has similar switch-action with four-switch buck–boost (FSBB) converter and bidirectional buck/boost, this work uses partial switch sharing to optimize the circuit topology. Fig. 2 shows the proposed HB^2-DAHB converter, by multiplexing two voltage regulation half-bridges on the basis of DAHB circuit topology.

The proposed converter contains half-bridges HB$_1$–HB$_3$, inductors L_1, L_2, and L_r, energy transfer transformer T, and half-bridge capacitors C_1–C_4. HB$_1$ is the front buck half-bridge, and HB$_2$ and HB$_3$ are the sharing half-bridges. Half-bridges HB$_1$, HB$_2$, and inductor L_r form the FSBB circuit, plays role in regulating voltage. HB$_2$, HB$_3$, inductor L_r, and transformer T forms voltage-fed DAHB circuit, which transfers the energy. The multiplexing half-bridge HB$_3$ and inductor L_2 constitute a bidirectional buck–boost circuit to realize half-voltage output. Half-bridge capacitors C_1–C_4 are used to generate square wave and maintain the stability of each bus voltage. Compared with other cascaded circuits, the proposed converter has less switches and no decoupling capacitors.

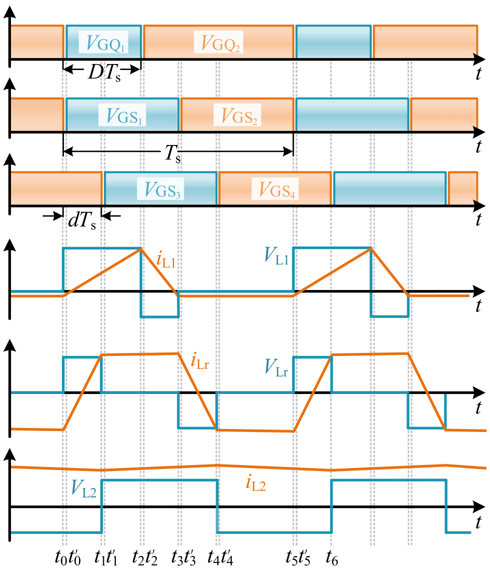

Fig. 3. Key waveforms of driving signal, voltage, and current.

This HB^2-DAHB converter adopts a hybrid control method combining pulsewidth modulation (PWM) and phase-shift modulation (PSM), including two control degrees: D and d. D is the duty ratio of the switch Q_1 in the half-bridge HB$_1$, which can adjust the input voltage of DAHB circuit and expand the voltage gain range. d represents the phase-shift ratio between the half-bridges HB$_2$ and HB$_3$, which controls the magnitude and direction of energy transmission. The system has four voltage levels, as high voltage V_1 and V_2, and low voltage V_3 and V_4, suitable for dc batteries and loads of different voltage levels in EVs.

B. Operation Analysis

Taking the forward mode as an example to analyze the operation mode of the HB^2-DAHB converter. The switches on each half-bridge are conducted complementarily. The circuit operates in a step-down state, and the duty cycle D is less than 0.5. The duty cycle of switches in half-bridges HB$_2$ and HB$_3$ is kept at 0.5. The key voltage and current waveforms in the circuit are shown in Fig. 3. There are five operation modes in one steady-state switching period.

To simplify the circuit modal analysis, the following assumptions are made.

1) The loss of passive devices during charging and discharging progress is ignored.
2) The half-bridge capacitors C_1–C_4 are large, and the voltage across these capacitors is stable.
3) The dead time t_d is added to avoid short-circuited, and the resonance process of the inductor and switch parasitic capacitor in the dead time t_d is ignored.

Fig. 4 shows the corresponding equivalent circuit of each mode. The turn-OFF time t_0 of switch Q_2 is taken as the starting point of the operation analysis and the phase of S_1 is taken as the initial zero phase. The positive direction of inductor current is from the input side to the output side.

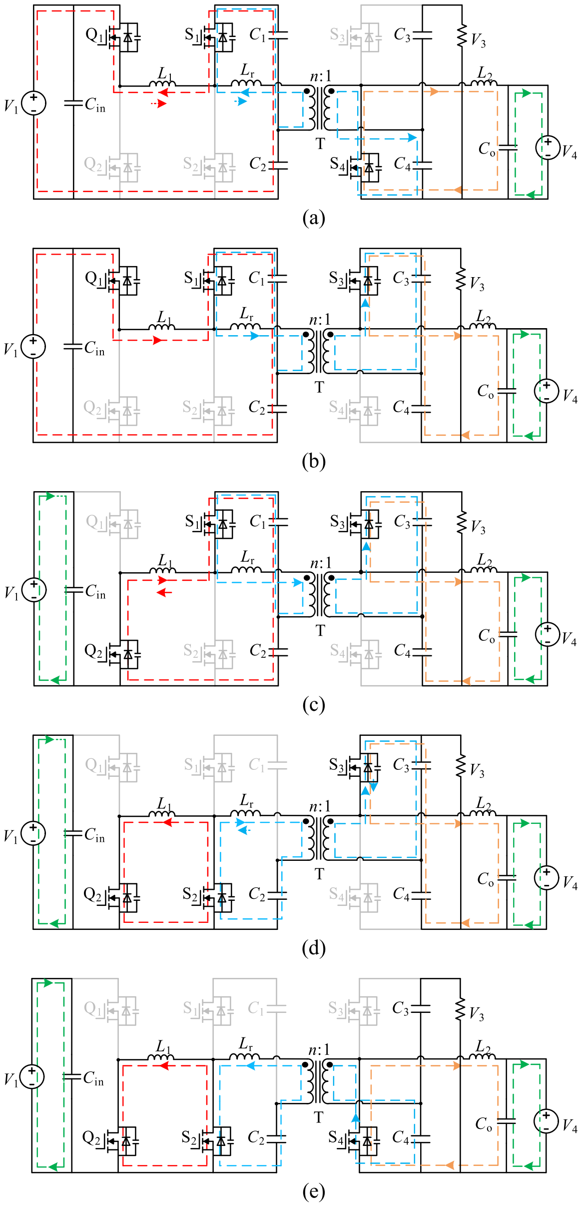

Fig. 4. Equivalent circuit of the proposed converter in forward mode. (a) Mode 1 [t_0, t_1]. (b) Mode 2 [t_1, t_2]. (c) Mode 3 [t_2, t_3]. (d) Mode 4 [t_3, t_4]. (e) Mode 5 [t_4, t_5].

Mode 1 [t_0, t_1]: During the period $t_0 - t_0'$, half-bridge HB$_1$ and HB$_2$ enter the dead time. The reverse current flowing through inductor L_1 charges and discharges the parasitic capacitors of the switches Q_1 and Q_2. Before time t_0', the parasitic capacitor of switch Q_1 is completely discharged, achieving ZVS turn-ON. Similarly, under the combined action of the inductor currents i_{Lr} and i_{L1}, the switch S_1 realizes ZVS turn-ON.

After switches Q_1 and S_1 turned ON, the half-bridge circuits HB$_1$ and HB$_2$ form the buck circuit and maintain the voltage stability at the DAHB circuit input side. V_1 transfers energy to the DAHB circuit through the inductor L_1. The inductor L_2 and capacitor C_o perform LC filtering to maintain the stability of the output voltage. In this mode, the reverse current i_{Lr} charges the parasitic capacitor C_{oss1} of switch S_1 and the half-bridge capacitors C_1 and C_4. In this mode, the current flowing through the inductor L_r is calculated as

$$i_{L_\mathrm{r}}(t) = i_{L_\mathrm{r}}(t_0) + \frac{V_2 + nV_3}{2L_\mathrm{r}}(t - t_0) \tag{1}$$

where n is the turns ratio, V_2 and $V_{3,}$ respectively, represent the primary and secondary voltages of the DAHB circuit, and $i_{\mathrm{Lr}}(t_0)$ corresponds to the inductor current i_{Lr} at time t_0. At time t_1, the inductor current $i_{\mathrm{Lr}}(t_1)$ is calculated as

$$i_{L_\mathrm{r}}(t_1) = i_{L_\mathrm{r}}(t_0) + \frac{V_2 + nV_3}{4L_\mathrm{r}f}d. \tag{2}$$

d is calculated as $d = \varphi/180°$, φ is the phase-shift angle between switches S_1 and S_3.

Mode 2 [t_1, t_2]: At time t_1, switch S_4 turns OFF. Under the combined action of the inductor currents i_{Lr} and i_{L2}, the current flowing through switch S_3 discharges its parasitic capacitor, and the body diode is turned ON. At time $t_1{}'$, voltage-clamped switch S_3 achieves ZVS turn-ON. V_1 transfers energy to the output load through L_1, L_r, and L_2. In Modes 1 and 2, the current flowing through the energy storage inductor L_1 is calculated as

$$i_{L_1}(t) = I_1 + \frac{V_1 - V_2}{L_1}(t - t_0) \tag{3}$$

where I_1 represents circulating current of the inductor L_1 in Mode 4 and Mode 5.

At time t_2, the inductor current $i_{\mathrm{L1}}(t_2)$ is calculated as

$$i_{L_1}(t_2) = I_1 + \frac{V_1 - V_2}{L_1 f}D. \tag{4}$$

Mode 3 [t_2, t_3]: At time t_2, the front stage half-bridge circuit HB_1 enters the dead time. The forward current i_{L1} discharges the parasitic capacitor of the switch Q_2 and realizes the ZVS turn-ON. The energy stored in the inductor L_1 is transferred to the DAHB circuit through the path formed by the switches Q_2 and S_1, maintaining the bus voltage V_2 stability.

The output energy of the DAHB circuit is transferred to the load through the switch S_3 and the inductor L_2. In this mode, the current flowing through the energy storage inductor L_1 is

$$i_{L_1}(t) = i_{L_1}(t_2) - \frac{V_2}{L_1}(t_3 - t_2). \tag{5}$$

At time t_3, the inductor current $i_{\mathrm{L1}}(t_3)$ is calculated as

$$i_{L_1}(t_3) = I_1 + \frac{V_1 - V_2}{L_1 f}D - \frac{V_2}{2L_1 f}(1 - 2D). \tag{6}$$

In Modes 2 and 3, under the control of the front and rear voltage regulator circuits, the voltage difference across the inductor L_r is $(V_2\_nV_3)/2$, approximately the matching state. The current flowing through the inductor L_r is calculated as

$$i_{L_\mathrm{r}}(t) = i_{L_\mathrm{r}}(t_1) + \frac{V_2 - nV_3}{2L_\mathrm{r}}(t - t_2). \tag{7}$$

At time t_3, the inductor current $i_{\mathrm{Lr}}(t_3)$ is calculated as

$$i_{L_\mathrm{r}}(t_3) = i_{L_\mathrm{r}}(t_0) + \frac{V_2 + nV_3}{4L_\mathrm{r}f}d + \frac{V_2 - nV_3}{4L_\mathrm{r}f}(1 - d). \tag{8}$$

Mode 4 [t_3, t_4]: At the beginning of this mode, half-bridge circuit HB_2 enters dead time. Under the combined action of the inductor currents i_{L1} and i_{Lr}, the body diode of the switch S_2 is turned ON, and the voltage across S_2 is clamped to zero. At time $t_3{}'$, the drive signal arrives, and switch S_2 realizes ZVS turn-ON. In this mode, the inductor L_1 freewheels through the loop formed by the switches Q_2 and S_2, and the circulating current is defined as I_1. The energy stored by inductor L_r is transferred to the output side and the voltage across the inductor L_r is $(-V_1 - nV_2)/2$.

The current flowing through the inductor L_r is calculated as

$$i_{L_\mathrm{r}}(t) = i_{L_\mathrm{r}}(t_3) + \frac{-V_2 - nV_3}{2L_\mathrm{r}}(t - t_3). \tag{9}$$

At time t_4, the inductor current $i_{\mathrm{Lr}}(t_4)$ is calculated as

$$i_{L_\mathrm{r}}(t_4) = i_{L_\mathrm{r}}(t_0) + \frac{V_2 - nV_3}{4L_\mathrm{r}f}(1 - d). \tag{10}$$

In Modes 2 to 4, the voltage across the inductor L_2 is maintained at V_3–V_4. And the current flowing through the inductor L_2 is

$$i_{L_2}(t) = i_{L_2}(t_1) + \frac{V_3 - V_4}{L_2}(t - t_1). \tag{11}$$

At time t_4, the inductor current $i_{\mathrm{L2}}(t_4)$ is calculated as

$$i_{L_2}(t_4) = i_{L_2}(t_1) + \frac{V_3 - V_4}{2L_2 f}d. \tag{12}$$

Mode 5 [t_4, t_5]: In this mode, the proposed converter enters intermittent operation mode. The energy storage element in the circuit maintains the output voltage stability. At time t_4, switch S_3 turns OFF. The inductor current i_{Lr} and the current i_{L2} jointly discharge the parasitic capacitor of the switch S_3. After the parasitic capacitor is completely discharged, switch S_3 can realize ZVS turn-ON. The front circuit maintains continuous circulating current state. In this mode, the voltage across the inductor L_2 is $-V_4$ and the current flowing through inductor L_2 can be expressed as

$$i_{L_2}(t) = i_{L_2}(t_4) + \frac{-V_4}{L_2}(t - t_4). \tag{13}$$

At time t_4, the inductor current $i_{\mathrm{L2}}(t_4)$ is calculated as

$$i_{L_2}(t_5) = i_{L_2}(t_1) + \frac{V_3}{2L_2 f} - \frac{V_4}{L_2 f}. \tag{14}$$

Half-bridge capacitors C_2 and C_4 charge the inductor L_r, and the voltage across the inductor L_r is $(-V_2 + nV_3)/2$. The current flowing through the inductor L_r is calculated as

$$i_{L_\mathrm{r}}(t) = i_{L_\mathrm{r}}(t_4) + \frac{-V_2 + nV_3}{2L_\mathrm{r}}(t - t_4). \tag{15}$$

After the end of Mode 5, the converter starts to operate periodically in steady state. When the converter operates in reverse mode, extended half-bridges HB_1 and HB_3 constitute the boost unit, respectively. The operation process of the system in the forward and reverse directions is symmetrical, so the detailed explanation of the boost mode is omitted.

III. CIRCUIT CHARACTERISTIC ANALYSIS

A. Analysis of the Output Characteristic

According to the modal analysis in Section II, when the system operates stably and the periodic stability condition of inductor current i_{L1} and i_{L2} is

$$i_{L_1}(t_0) = i_{L_1}(t_3), i_{L_2}(t_0) = i_{L_2}(t_5). \tag{16}$$

Therefore, the voltage gain between different voltage level dc buses can be calculated as

$$V_4/V_1 = 2D_1, V_4/V_3 = 0.5. \tag{17}$$

The overall voltage gain of the system is calculated as

$$\frac{V_4}{V_1} = \frac{DV_3}{V_2} = \frac{D}{nk} \tag{18}$$

where $k = V_2/nV_3$ represents the voltage matching ratio of the DAHB circuit. According to formula (18), the voltage gain of HB^2-DAHB converter is significantly increased. Compared with the traditional DAHB or DAB converter, the gain range of the HB^2-DAHB converter can be widened by 0.1–9 times.

Because of the voltage stabilizing effect of the half-bridge capacitor C_1–C_4, the dc bus V_2 and V_3 can be regarded as two constant voltage outputs. Therefore, the converter can be regarded as a combination of two voltage sources and power source. The output power of the low-voltage ports V_3 and V_4 is determined by the DAHB circuit. The inductor L_{r} plays the role of energy storage and energy transfer. Integrating the inductor current i_{Lr} in each mode, the output power of the DAHB circuit can be calculated as

$$P_{\mathrm{o}} = \frac{2}{T}\int_0^{t_3} \frac{V_2 i_{\mathrm{Lr}}(t)}{2} dt = \frac{nV_1V_4D}{2L_{\mathrm{r}}f} d(1-d). \tag{19}$$

By adding the duty cycle D as the control degree of freedom, the control flexibility of the DAHB circuit can be optimized. Compared with the traditional DAHB or DAB converter, the proposed converter extends the voltage gain of the system, reduces the voltage stress of the inductor L_{r}, and optimizes the voltage-matching state of the primary and secondary sides of the inductor L_{r}.

B. Analysis of the Soft-Switching Characteristic

Under the condition of high voltage gain, the large voltage difference leads to the distortion of inductor current waveform, and some switches would loss ZVS turn-ON. Therefore, extending the soft-switching range of the converter under high-gain conditions is of great significance for maintaining the EV's dc bus stability and high-efficiency bidirectional transmission. The principle of ZVS turn-ON is that the parasitic capacitor of switch is completely discharged during the dead time before the arrival of the drive signal. Taking the current polarity as the criterion, the soft-switching range of each switch is discussed as follows.

By integrating the inductor current i_{L1} during the turn-ON time of S_1, the circulating current I_1 in Mode 4 to Mode 5 can be calculated as

$$I_1 = \frac{nV_4}{2L_{\mathrm{r}}f} d(1-d) + \frac{V_1D(2D-1)}{2L_1f}. \tag{20}$$

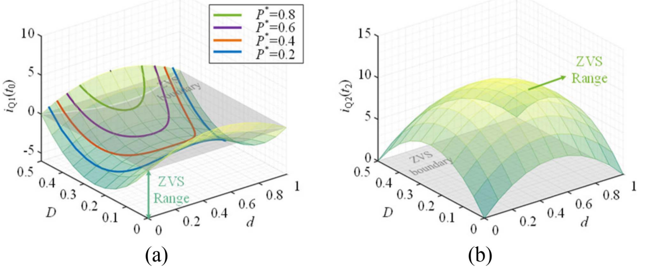

Fig. 5. Soft-switching range of Q_1 and Q_2 under different D and d conditions. (a) Soft-switching range of Q_1. (b) Soft-switching range of Q_2.

Similarly, the initial current of the inductor current i_{L2} is

$$I_2 = \frac{nV_1D}{2L_{\mathrm{r}}f} d(1-d) - \frac{V_4}{4L_2f}. \tag{21}$$

The current of switches Q_1 and Q_2 at the turn-ON time are

$$\begin{cases} i_{\mathrm{Q}_1}(t_0) = \frac{nV_4}{2L_{\mathrm{r}}f} d(1-d) - \frac{V_1D(1-2D)}{2L_1f} \\ i_{\mathrm{Q}_2}(t_2) = \frac{nV_4}{2L_{\mathrm{r}}f} d(1-d) + \frac{V_1D(1-2D)}{2L_1f} \end{cases}. \tag{22}$$

Fig. 5 shows the soft-switching range of switches Q_1 and Q_2 under different D and d conditions. Due to the continuous flow effect of inductor L_1, switch Q_2 can be able to realize the ZVS turn-ON under different conditions, showing good soft-switching characteristics. The soft-switching condition of switch Q_1 is related to the transmission power and the buck ratio of HB$_1$, corresponding to the control variables d and D. Fig. 5(a) compares the influence of D on the soft-switching range of Q_1 under specific power conditions and Q_1 has the largest ZVS turn-ON range around $D = 0.25$. Combined with the transmission power characteristics of the system, Q_1 has better soft-switching characteristics under light-load condition. With the transmission power P_{o} of the system increases, the circulating current I_1 increases, and the ZVS range of the Q_1 decreases. This result limits the load-carrying capability of the high-voltage side V_2.

The half-bridge HB$_2$ and HB$_3$ in the DAHB circuit are used as sharing circuit arms, and the soft-switching conditions of switches S_1–S_4 are jointly determined by multiple inductor currents. Under steady-state conditions, the average current flowing through the inductor L_{r} is zero during one switching cycle, and the current i_{Lr}(t) at the initial moment t_0 is calculated as

$$i_{L_{\mathrm{r}}}(t_0) = -\frac{nV_4(2d-1) + D_1V_1}{4L_{\mathrm{r}}f}. \tag{23}$$

Based on the formulas (20), (21), and (23), the currents of switches S_1–S_4 at the turn-ON time are calculated as follows:

$$\begin{cases} i_{\mathrm{S}_1}(t_0) = \frac{nV_{\mathrm{out}}D_2}{4L_{\mathrm{r}}f}(1-4d+2d^2) - \frac{V_{\mathrm{in}}D_1}{4}(\frac{1}{L_{\mathrm{r}}f} + \frac{4D_1-2}{L_{\mathrm{m1}}f}) \\ i_{\mathrm{S}_2}(t_3) = \frac{nV_{\mathrm{out}}D_2}{4L_{\mathrm{r}}f}\left(1-2d^2\right) + \frac{V_{\mathrm{in}}D_1}{4}\left(\frac{4D_1-2}{L_{\mathrm{m1}}f} - \frac{1}{L_{\mathrm{r}}f}\right) \\ i_{\mathrm{S}_3}(t_1) = \frac{nV_{\mathrm{in}}D_1}{4L_{\mathrm{r}}f}\left(2d^2-1\right) + \frac{n^2V_{\mathrm{out}}}{4}\left(\frac{D_2}{L_{\mathrm{r}}f} + \frac{2D_2-1}{n^2L_{\mathrm{m2}}f}\right) \\ i_{\mathrm{S}_4}(t_4) = \frac{nV_{\mathrm{in}}D_1}{4L_{\mathrm{r}}f}\left(1-4d+2d^2\right) - \frac{n^2V_{\mathrm{out}}}{4}\left(\frac{D_2}{L_{\mathrm{r}}f} + \frac{2D_2-1}{n^2L_{\mathrm{m2}}f}\right) \end{cases}. \tag{24}$$

According to formula (24), Fig. 6 shows the soft-switching range of switches S_1–S_4, respectively. The Z-axis represents the

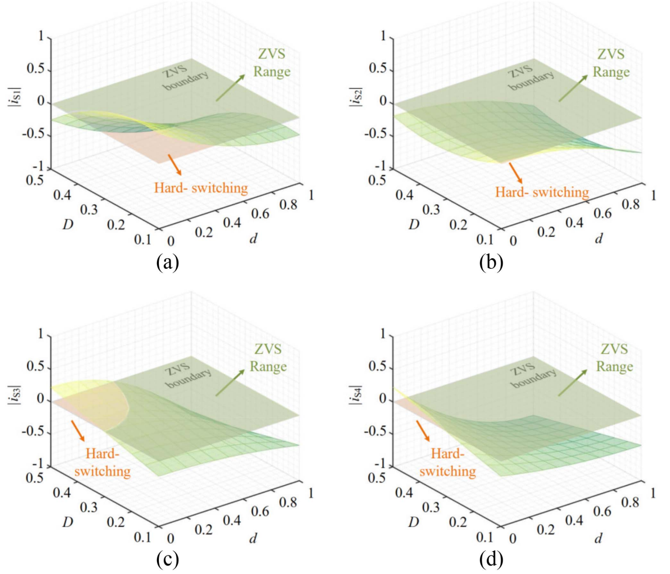

Fig. 6. Soft-switching range of switches S_1–S_4 under different D and d conditions. (a) Soft-switching range of S_1. (b) Soft-switching range of S_3. (c) Soft-switching range of S_3. (d) Soft-switching range of S_4.

polarity of the switching current at the turn-ON time, and the reverse switching current can achieve soft switching. Due to the continuous flow effect of inductors L_1 and L_2, shared switches S_2, S_3, and S_4 have a wider soft-switching range, which can achieve ZVS turn-ON under full-power range. Combined with the transmission power, the soft-switching range of switch S_1 decreases under light-load condition. By adjusting the duty cycle D to realize the voltage matching of the DAHB circuit, the shared switches S_1–S_4 can realize ZVS turn-ON in a wide load range.

C. Analysis of the Inductor Current Stress

Inductor current stress is the maximum current flowing through each inductor during periodic steady-state operation, which always occurs at the inflection point of switching state transitions. The current stress of each inductor is calculated as follows. Correspondingly, the change of the inductor current stress is shown in Fig. 7

$$I_{L_1-\max} = i_{L_1}(t_2) = \frac{nV_4}{2L_{\mathrm{r}}f}d(1-d) + \frac{V_1 D(1-2D)}{4L_1 f} \tag{25}$$

$$I_{L_2-\max} = i_{L_2}(t_4) = \frac{nV_1 D}{2L_{\mathrm{r}}f}d(1-d) + \frac{V_4}{4L_2 f} \tag{26}$$

$$I_{L_{\mathrm{r}}-\max} = \begin{cases} i_{L_{\mathrm{r}}}(t_1) = \frac{V_1 D_1(2d-1)+nV_4}{4L_{\mathrm{r}}f} & \frac{V_1}{nV_4} < \frac{1}{D_1} \\ i_{L_{\mathrm{r}}}(t_3) = \frac{nV_4(2d-1)+DV_1}{4L_{\mathrm{r}}f} & \frac{V_1}{nV_4} \geq \frac{1}{D_1} \end{cases}. \tag{27}$$

As shown in Fig. 7(a), the current stress of inductor L_1 shows a quadratic function with the duty ratio D, and reaches the maximum at $D = 0.25$. According to Fig. 7(b), the current stress of inductor L_2 is mainly related to the output power of the low voltage V_4 port and inductance value. Under the same transmission power condition, the stress of current i_{L2} is independent of D and d. The current stress of the inductor current i_{Lr} divides two curved surfaces according to whether the primary and secondary voltages of the DAHB circuit are matched. As shown in Fig. 7(c), the simulation parameters are set to be the voltage matching state when $D = 0.3$. Under the same transmission power condition, i_{Lr} reaches the minimum value at the voltage matching state.

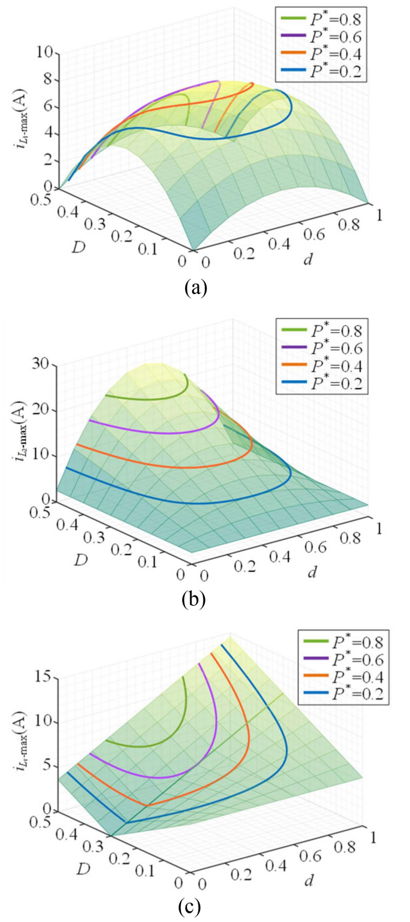

Fig. 7. Variation surface graph of the current stress of each inductor. (a) Current stress of inductor L_1. (b) Current stress of inductor L_2. (c) Current stress of inductor L_{r}.

D. Analysis of the Reactive Backflow Loss

During the operation of Mode 2, the input voltage and current in opposite phases generate reactive backflow loss, which is the necessary condition to realize ZVS turn-ON of switch Q_1. As an inherent problem of the traditional DAB and DAHB converter, reactive backflow loss Q_{re} is not transferred to the output load, which would increase the current stress in the circuit and reduce the system efficiency. Especially at high-gain conditions, large reactive backflow loss would cause voltage fluctuation and harmonic contamination problems in the dc bus, affecting the safe and stable operation of EVs.

According to the modal analysis in Section II, the reactive backflow energy in this DAHB circuit charges the half-bridge capacitors C_1 and C_2, which can maintain the voltage stability of the DAHB circuit. In addition, because of the freewheeling effect of inductor L_1, the reactive backflow loss can be further reduced under full-load condition. The reactive backflow loss of

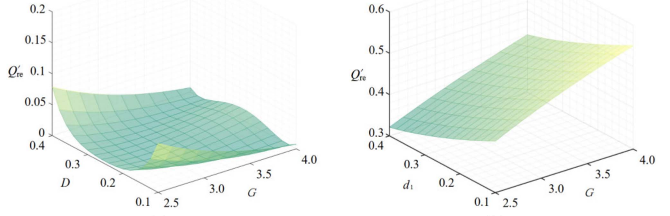

(a) (b)

Fig. 8. Comparison of the reactive backflow loss ratio under different voltage gain conditions. (a) HB^2-DAHB converter. (b) DAB converter.

the proposed converter can be calculated as

$$Q_{\rm re} = \frac{L_1 f}{8(1-2D)}\left[\frac{V_1 D(2D-1)}{L_1 f} + \frac{nV_4 d(1-d)}{L_{\rm r} f}\right]^2. \quad (28)$$

Fig. 8 shows the variation of the reactive backflow loss ratio $Q'_{\rm re}$ of the HB^2-DAHB converter and the traditional DAB converter, under the same parameter conditions. $Q'_{\rm re}$ is defined as the proportion of reactive backflow loss to the active output power, which can intuitively reflect the influence of reactive backflow loss on system efficiency. And $G = V_1/nV_4$ represents the voltage gain of the circuit structure without transformer. Similar to the converter designed in this work, the DAB converter is adopted on extend phase-shift control, which mainly adjusts the magnitude and direction of the energy transfer through interbridge phase shift d, and optimizes the circuit characteristics by in-bridge phase shift d_1.

In the comparative analysis shown in Fig. 8, the reactive backflow loss accounts for a less proportion in the proposed HB^2-DAHB converter, especially under high-gain condition. On the contrary, due to the serious voltage mismatch state, traditional DAB and DAHB converter have larger reactive backflow loss, which seriously would affect the efficiency and security of the system. This result proves that the proposed HB^2-DAHB converter shows advantages and potential in the application of low turn ratio and high gain.

IV. EXPERIMENTAL VERIFICATION

A. Parameter Design

According to the analysis of soft-switching characteristics in Section III, switches Q_2, S_2, S_3, and S_4 can realize ZVS turn-ON in a wide load range. While, the soft-switching ranges of switches Q_1 and S_1 show an opposite trend with load changes. To expand the soft-switching range, the optimization design of inductance parameters is necessary. When the voltages on the primary and secondary sides of transformer are matched, as $V_2 = nV_3$ the soft-switching conditions of switches Q_1 and S_1 and the reactive loss ratio $Q'_{\rm re}$ the can be simplified as

$$\begin{cases} Q_1: \frac{d(1-d)}{1-2D} \leq \frac{L_{\rm r}}{L_1} \\ S_1: \frac{d(1-d)}{1-2D} \geq \frac{L_{\rm r}}{L_1} \\ Q'_{\rm re} = \frac{(1-2D)}{4d(1-d)}\frac{L_{\rm r}}{L_1} + \frac{d(1-d)}{4(1-2D)}\frac{L_1}{L_{\rm r}} - \frac{1}{2} \end{cases}. \quad (29)$$

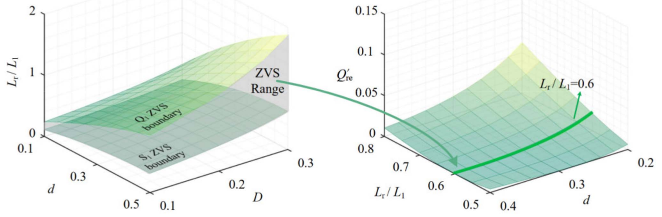

(a) (b)

Fig. 9. Influence of inductance parameter ratio $L_{\rm r}/L_1$ on soft switching and reactive backflow loss. (a) Effect of $L_{\rm r}/L_1$ on ZVS range of switches Q_1 and S_1. (b) Effect of $L_{\rm r}/L_1$ on reactive backflow loss ratio $Q'_{\rm re}$.

TABLE II
PROTOTYPE PARAMETER

Parameter	Value
HV dc Bus V_1	400 V
HV dc Bus V_2	240 V
LV dc Bus V_3	48 V
LV dc Bus V_4	24 V
Rated power $P_{\rm out}$	500 W
Switching Frequency f	100 kHz
Transformer Turns Ratio n:1	5:1
Energy Storage inductor L_1	47 μH
Energy Storage inductor L_2	47 μH
Leakage inductor $L_{\rm r}\times n^2$	33 μH
Energy storage capacitor C_1–C_4	200 μF

Fig. 9 shows the influence of inductance parameter ratio $L_{\rm r}/L_1$ on soft-switching range of switches Q_1 and S_1, and the reactive backflow loss ratio $Q'_{\rm re}$ under the condition of voltage matching state. According to Fig. 9(a), when the inductance ratio $L_{\rm r}/L_1$ is in the range of 0.6–0.8, the HB^2-DAHB converter has a wide soft-switching range and low reactive backflow loss, showing a high performance. Considering the transmission power of the system and the volume of magnetic components, the design of inductance value can be designed.

According to the voltage value of each port, the transformer turns ratio n is set to 5:1, to achieve better voltage matching state. Considering the values of the common power inductors, inductors L_1, L_2, and $L_{\rm r}$ are selected as 47, 47, and 33 μH, respectively. For better voltage regulation, capacitors C_1–C_4 are designed to be 200 μF. The parameters of the HB^2-DAHB converter are shown in Table II. Port V_3 and port V_4 are two low-voltage dc output terminals, which can be connected with EV's on-bored dc electronic equipment and storage batteries of different voltage levels.

B. Control Strategy

The system adopts a hybrid control method combining PWM and PSM, and the control block diagram is shown in Fig. 10. Due to the half-voltage output relationship between V_3 and V_4, the system only needs to sample voltages V_2 and V_3. According to the sampling value V_{2_s} and V_{3_s}, the duty cycle D of HB_1 can be determined by the voltage regulator (classical PI algorithm modules). According to the voltage sampling value V_{3_s} and reference value V_{3_ref}, the output voltage regulator generates the

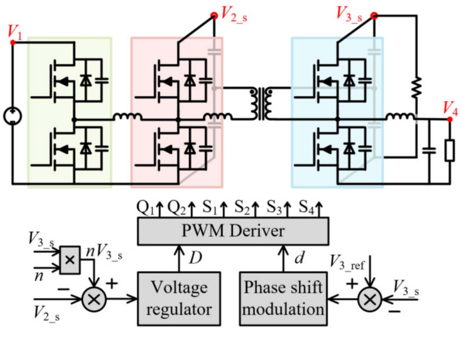

Fig. 10. Control block diagram of the system.

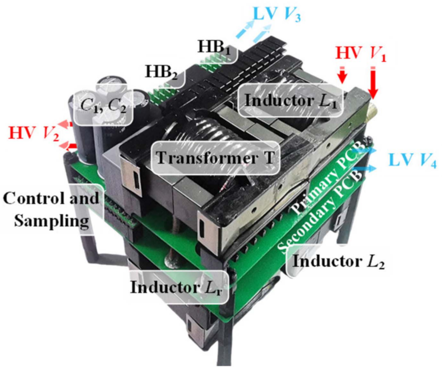

Fig. 11. Diagram of the experimental prototype.

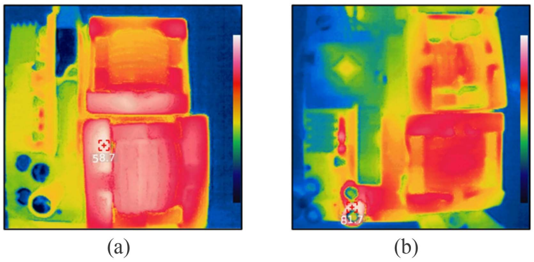

(a) (b)

Fig. 12. Thermal image of the experimental prototype. (a) Heat generation of the primary side circuit. (b) Heat generation of the secondary side circuit.

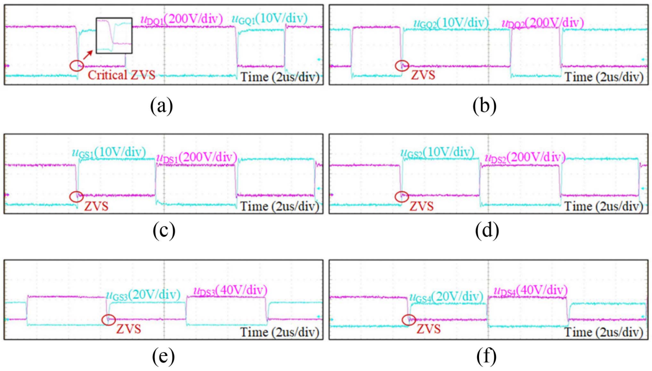

(a) (b) (c) (d) (e) (f)

Fig. 13. Soft-switching waveforms of each switch under rated operation mode. ($P_{48\mathrm{V}} = 250$ W, $P_{24\mathrm{V}} = 250$ W). (a) Soft switching of switches Q_1. (b) Soft switching of switches Q_2. (c) Soft switching of switches S_1. (d) Soft switching of switches S_2. (e) Soft switching of switches S_3. (f) Soft switching of switches S_4.

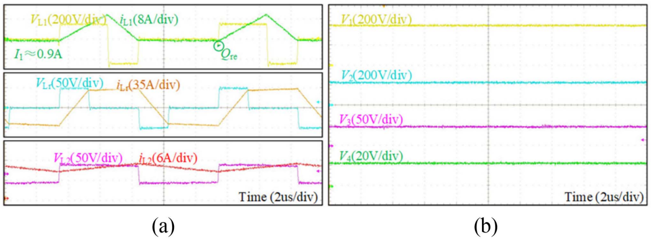

(a) (b)

Fig. 14. Voltage and current waveforms of each inductor and system output under rated mode. ($P_{48\mathrm{V}} = 250$ W, $P_{24\mathrm{V}} = 250$ W). (a) Voltage and current waveform of each inductor. (b) Voltage waveform of each port.

phase shift d. Finally, the PWM signal generator generates the pulse signal for the HB^2-DAHB converter to drive the switch ON and OFF. The proposed hybrid control strategy is simple, with two classical PI algorithm modules, and can be implemented online in common microprocessors.

C. Experimental Results

According to the optimized design of parameters, a 500 W principle prototype was built and tested to verify the good performance of proposed converter under high-voltage-gain conditions. The experimental prototype is shown in Fig. 11. The prototype adopts a 3-D vertical structure, the primary side circuit is on the top layer, and the secondary side circuit is on the bottom layer. The size of the experimental prototype is 8.4 cm × 8.4 cm × 8.5 cm, and the power density of the system is about 14.9 W/in^3.

By adjusting the duty cycle D of the extended half-bridge HB_1, the primary and secondary sides of the DAHB circuit are designed as the matching state, which can achieve better soft-switching characteristics, minimal current stress, and reactive backflow loss. Through single-phase-shift control, the poststage DAHB circuit transmits full-load power to the dual low-voltage output sides. The performance of the converter is verified by related experiments as follows.

Fig. 12 shows the thermal image of primary and secondary circuits of the experimental prototype under stable operation conditions. Through natural heat dissipation, the operating temperature of the switches is around 70 °C. The temperature of each device in the prototype is below the rated maximum temperature, and the circuit works reliably.

Figs. 13 and 14 show the experimental waveforms under rated working condition, that is, the 48 V port and the 24 V port output 250 W, respectively. According to the soft-switching waveform, it can be seen that all the switches achieve ZVS turn-ON. It should be pointed out that due to the large parasitic capacitor, the switch Q_1 is in a critical soft-switching state. Fig. 14(a) shows the voltage and current waveforms of each inductor. The converter operates in the voltage matching state, with small reactive backflow loss and less current stress. The reverse circulating current I_1 of inductor L_1 is about 0.7 A, using to implement ZVS turn-ON for Q_1. According to the Fig. 12(b), the voltage of the three ports is stable, and the high step-down capability is achieved under the condition of low turn ratio. Similarly, Figs. 15–18 conduct

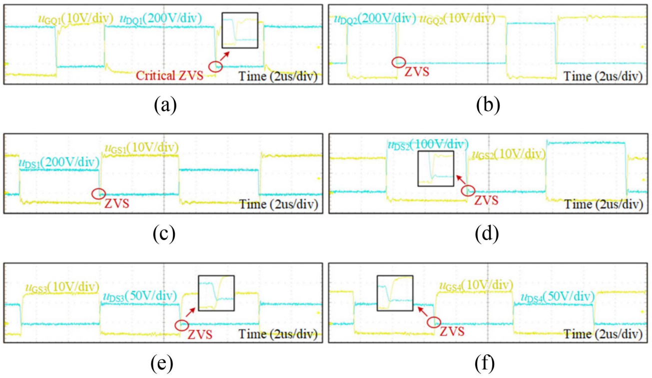

(a) (b)
(c) (d)
(e) (f)

Fig. 15. Soft-switching waveforms of each switch under the condition of $P_{48\text{V}} = 500$ W, $P_{24\text{V}} = 0$ W. (a) Soft switching of switches Q_1. (b) Soft switching of switches Q_2. (c) Soft switching of switches S_1. (d) Soft switching of switches S_2. (e) Soft switching of switches S_3. (f) Soft switching of switches S_4.

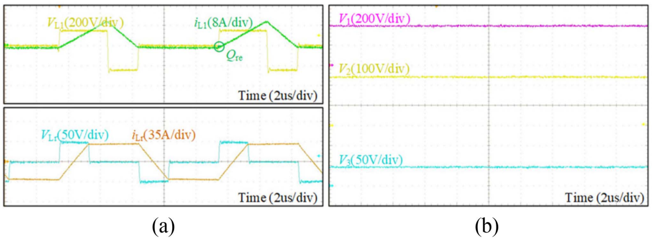

(a) (b)

Fig. 16. Voltage and current waveforms of each inductor and system output under the condition of $P_{48\text{V}} = 500$ W, $P_{24\text{V}} = 0$ W. (a) Voltage and current waveform of each inductor. (b) Voltage waveform of each port.

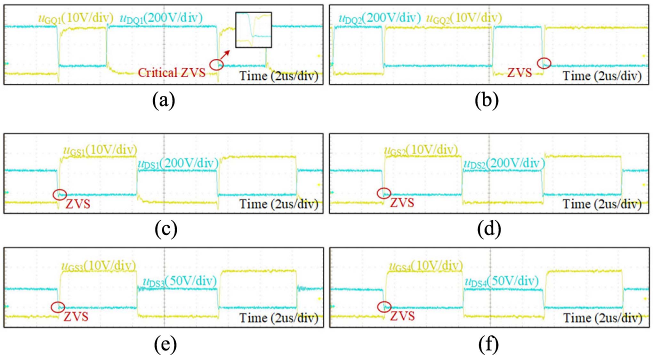

(a) (b)
(c) (d)
(e) (f)

Fig. 17. Soft-switching waveforms of each switch under the condition of $P_{48\text{V}} = 500$ W, $P_{24\text{V}} = 0$ W. (a) Soft switching of switches Q_1. (b) Soft switching of switches Q_2. (c) Soft switching of switches S_1. (d) Soft switching of switches S_2. (e) Soft switching of switches S_3. (f) Soft switching of switches S_4.

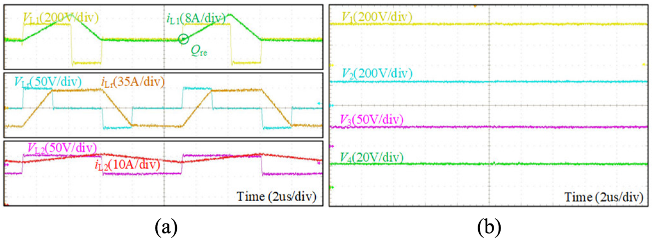

(a) (b)

Fig. 18. Voltage and current waveforms of each inductor and system output under the condition of $P_{48\text{V}} = 500$ W, $P_{24\text{V}} = 0$ W. (a) Voltage and current waveform of each inductor. (b) Voltage waveform of each port.

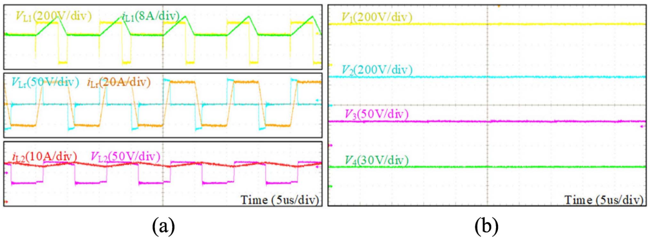

(a) (b)

Fig. 19. Voltage and current waveforms of each inductor and system output under conditions of $V_3 = 56$ V, $V_4 = 28$ V, $P_4 = 500$ W. (a) Voltage and current waveform of each inductor. (b) Voltage waveform of each port.

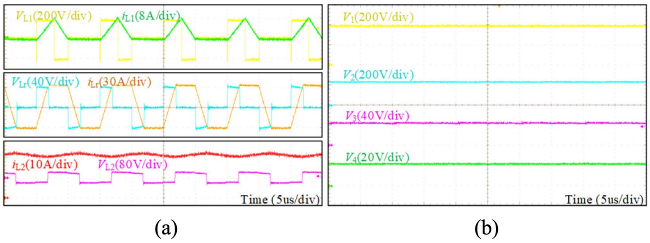

(a) (b)

Fig. 20. Voltage and current waveforms of each inductor and system output under conditions of $V_3 = 44$ V, $V_4 = 22$ V, $P_4 = 450$ W. (a) Voltage and current waveform of each inductor. (b) Voltage waveform of each port.

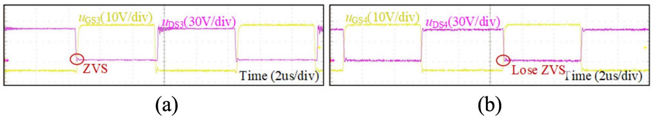

(a) (b)

Fig. 21. Soft-switching waveforms of switches S_3 and S_4 under reverse boost 24–48 V working mode. (a) Soft switching of switches S_3. (b) Soft switching of switches S_4.

comparative experiments to verify the performance of the experimental prototype under different power allocation conditions. Based on the optimized parameter design, the system has good soft-switching characteristics and low reactive backflow loss, consistent with theoretical analysis.

To prove the superiority of the HB^2-DAHB converter within a certain voltage range, Figs. 19 and 20 show the experimental waveforms when the output voltage V_4 is set to 28 V and 22 V, respectively. By adjusting the duty cycle D of the prestage circuit, the voltage across the inductor L_r can be maintained matching state. Each switch can achieve ZVS turn-ON, the current stress and reactive loss are relatively low.

In addition, the performance experiment of reverse boost mode is carried out. Fig. 21 shows the situation where the 24 V port directly supplies power to the 48 V port, simulating the application scenario where the low-voltage energy storage battery supplies power to the dc load. At this time, the transformer is disconnected, and the system operating mode is simple bidirectional buck/boost. Although switch S_2 does not implement soft switching, the system has higher efficiency due to lower conduction loss and magnetic loss. Figs. 22 and 23 show the experimental waveform under the reverse rated working condition, that is, the low-voltage 24 V port transmits rated power to the high-voltage 400 V port. Under the combined effect of the inductor current i_{Lr} and i_{L2}, the switch S_4 can

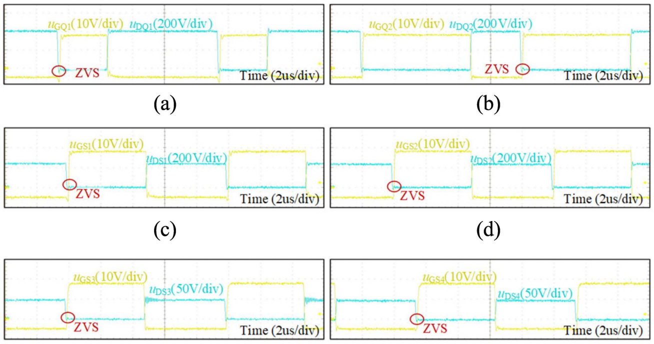

(a) (b) (c) (d) (e) (f)

Fig. 22. Soft-switching waveforms of each switch under reverse boost 24–400 V working mode. (a) Soft switching of switches Q_1. (b) Soft switching of switches Q_2. (c) Soft switching of switches S_1. (d) Soft switching of switches S_2. (e) Soft switching of switches S_3. (f) Soft switching of switches S_4.

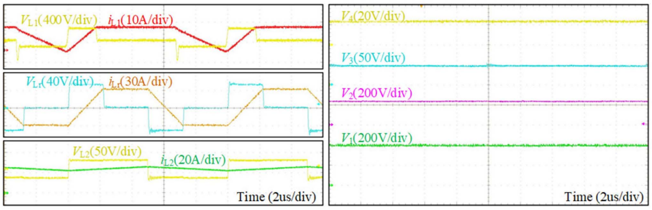

(a) (b)

Fig. 23. Voltage and current waveforms of each inductor and system output under reverse boost 24–400V working mode. (a) Voltage and current waveform of each inductor. (b) Voltage waveform of each port.

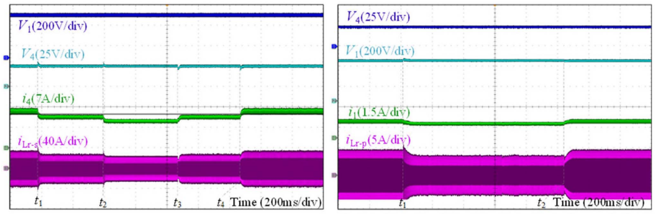

(a) (b)

Fig. 24. Dynamic response under the power step change. (a) Forward buck mode. (b) Reverse boost mode.

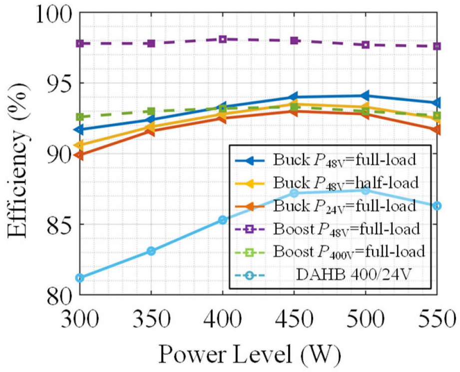

Fig. 25. Efficiency test curve of the experimental prototype.

realize ZVS turn-ON, and the system shows good soft-switching characteristics. Because of the freewheeling effect of inductor L_2, there is no reactive backflow loss in the system. The output voltage of each port is stable, which meets the boost requirement and conforms to the theoretical analysis.

Related experiments on the dynamic response under the output power step change are shown in Fig. 24. The initial conditions of the experiment are, $P_{48V} = 200$ W, $P_{24V} = 100$ W, and the load power of the 24 V port is constantly adjusted. In forward mode, P_{24V} is reduced from 300 W × 50 W to 200 W, and adjusted from 200 W back to 300 W. In reverse mode, P_{400V} is adjusted from 500 W to 400 W at time t_1, and adjusted back to 500 W at time t_2. The experimental results prove that when the power changes, the voltage at each port can remain stable without obvious fluctuations during the bidirectional energy transmission process.

Fig. 25 presents the efficiency curves in both the forward and reverse working modes under different load conditions. And Fig. 26 shows the test efficiency and losses distribution of the proposed converter under different power distribution conditions. Under the same parameter and device conditions, a DAHB experimental prototype was built for performance comparison. Because of the severe voltage mismatch state, inductor current i_{Lr} waveform is distorted, leading to large current stress, core loss and reactive backflow loss, and partial switches of DAHB circuit loses ZVS turn-ON. On the contrary, through the voltage regulation of the extended half-bridge HB_1, the proposed HB^2-DAHB converter can maintain the matching state and would have high efficiency under high-gain conditions.

The loss of the system mainly includes switching devices losses, magnetic component losses, circuit conduction loss, and other stray losses. The turn-ON loss of switches can be approximately ignored because of the good soft-switching characteristics. And the reactive loss can be manifested as an increase in conduction losses and magnetic losses. The peak efficiency in rated forward mode can reach about 94.1%, which corresponds to the situation where the 48 V port outputs full-load power. As the output power of the 24 V port increases, the efficiency of system decreases, because of additional conduction loss and magnetic loss. In the reverse boost mode, where V_4 directly transfers energy to V_3, the peak efficiency is about 98.1%, due to fewer devices in the circuit. When the V_4 port supplies power to the dc bus V_1, the test efficiency under rated conditions is about 93.4%. As the transmission power decreases, the ZVS range of the multiplexing switches might be narrowed, and the reactive loss of the system increases relatively, which would lead to lower efficiency and bus voltage fluctuations. Overall, the HB^2-DAHB converter is more suitable for full-load and half-load conditions.

Table III shows the performance comparison between the HB^2-DAHB converter and other bidirectional isolated dc–dc converters. The proposed converter can achieve high voltage gain under the condition of low turns ratio and fewer switches. Through the sharing of partial switches and the characteristics of two low-voltage output ports, the proposed converter has a simple structure and can improve the EV's space. Although the additional switches and inductors are added, the converter can improve the performance without significantly reducing the overall power density and increasing the system cost of the experimental prototype, because of the low-voltage stress of the primary switch and transformer and small magnetic core.

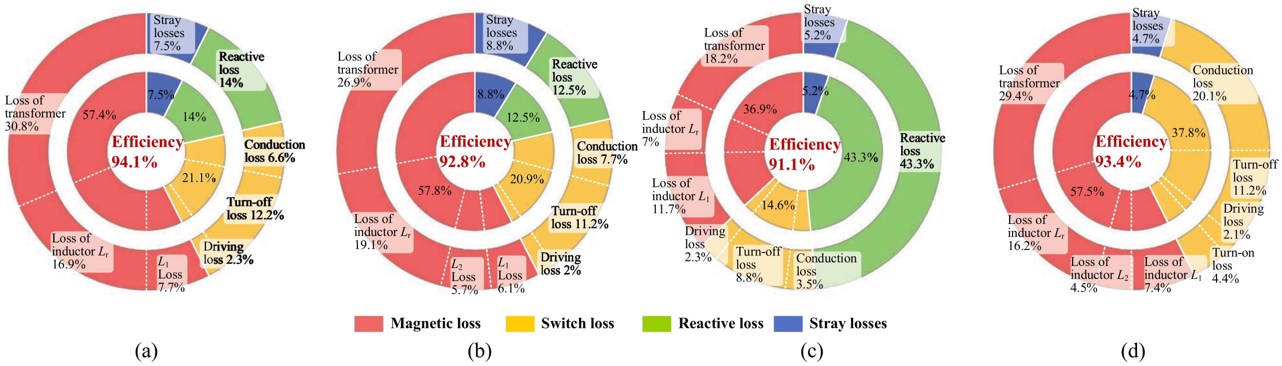

(a) (b) (c) (d)

Fig. 26. Experimental efficiency and losses distribution of the proposed converter. (a) Forward mode ($P_{48\text{V}} = 500$ W). (b) Forward mode ($P_{24\text{V}} = 500$ W). (c) Forward mode ($P_{24\text{V}} = 300$ W). (d) Reverse mode ($P_{400\text{V}} = 500$ W).

TABLE III
COMPARISON WITH OTHER OPTIMIZED BIDIRECTIONAL CONVERTERS

Converter	Input /Output Voltage	Frequency	Turns ratio	Switches	Magnetic elements	Power density	Power level	Test efficiency
[13]	400 V/50 V	1 MHz	8:2	12	4	≈ 21.6 W/in^3	500 W	93.0%
[15]	400 V/48 V	250 kHz	20:6	8	2	≈ 29.0 W/in^3	500 W	95.0%
[16]	380 V/48 V	50 kHz	40:10:10	6	4	——	1000 W	93.8%
[19]	400 V/48 V	40 kHz	21:10	6	4	≈ 9.43 W/in^3	500 W	94.1%
[22]	400 V/48 V	50 kHz	8.3:1	8	2	——	480 W	94.6%
[26]	400 V/48 V	200 kHz	—	8	4	≈ 15.2 W/in^3	1000 W	94.5%
Traditional DAHB	400 V/24 V	100 kHz	5:1	4	2	≈ 19.5 W/in^3	500 W	81.1%
This work	400 V/24 V	100 kHz	5:1	6	4	≈ 14.9 W/in^3	500 W	94.1%

V. CONCLUSION

On the basis of traditional DAHB converter, through partial switch sharing, this article proposes an optimized HB^2-DAHB converter with high gain and multiplexed output. Under the condition of fewer number of switches and less turn ratios, the proposed converter achieves higher buck–boost capability. Based on the circuit characteristic analysis and parameter optimization design, the principle prototype has been tested. And the experimental results verified the correctness of the theoretical analysis. The good soft-switching characteristics and low reactive backflow loss make the battery pack have high charge-discharge efficiency and service life. These advantages make the proposed converter show application potential in intelligent and automated EVs.

REFERENCES

[1] A. K. Singh, A. K. Mishra, K. K. Gupta, P. Bhatnagar, and T. Kim, "An integrated converter with reduced components for electric vehicles utilizing solar and grid power sources," *IEEE Trans. Transp. Electrific.*, vol. 6, no. 2, pp. 439–452, Jun. 2020.

[2] S. Jayalath and A. Khan, "Design, challenges, and trends of inductive power transfer couplers for electric vehicles: A review," *IEEE J. Emerg. Sel. Topics Power Electron.*, vol. 9, no. 5, pp. 6196–6218, Oct. 2021.

[3] X. Ma, P. Wang, Y. Wang, L. Tao, P. Cheng, and D. Zhao, "Variables decoupling and multi-objective optimization for high-power bidirectional interleaved converters in electric vehicles," in *Proc. IEEE Appl. Power Electron. Conf. Expo.*, 2022, pp. 1993–1999.

[4] A. Shafiqurrahman, B. S. Umesh, N. A. Sayari, and V. Khadkikar, "Electric vehicle-to-vehicle energy transfer using on-board converters," *IEEE Trans. Transp. Electrific.*, vol. 9, no. 1, pp. 1263–1272, Mar. 2023, doi: 10.1109/TTE.2022.3172029.

[5] H. Wang, S. Dusmez, and A. Khaligh, "Maximum efficiency point tracking technique for LLC-based PEV chargers through variable DC link control," *IEEE Trans. Ind. Electron.*, vol. 61, no. 11, pp. 6041–6049, Nov. 2014.

[6] C.-M. Lai, Y.-H. Cheng, M.-H. Hsieh, and Y.-C. Lin, "Development of a bidirectional DC/DC converter with dual-battery energy storage for hybrid electric vehicle system," *IEEE Trans. Veh. Technol.*, vol. 67, no. 2, pp. 1036–1052, Feb. 2018.

[7] B. Zhao, Q. Song, W. Liu, and Y. Sun, "Overview of dual-active-bridge isolated bidirectional DC–DC converter for high-frequency-link power-conversion system," *IEEE Trans. Power Electron.*, vol. 29, no. 8, pp. 4091–4106, Aug. 2014.

[8] H. Wang, S. Dusmez, and A. Khaligh, "Design and analysis of a full-bridge LLC-based PEV charger optimized for wide battery voltage range," *IEEE Trans. Veh. Technol.*, vol. 63, no. 4, pp. 1603–1613, May 2014.

[9] Y. Zhang, Y. Gao, L. Zhou, and M. Sumner, "A switched-capacitor bidirectional DC–DC converter with wide voltage gain range for electric vehicles with hybrid energy sources," *IEEE Trans. Power Electron.*, vol. 33, no. 11, pp. 9459–9469, Nov. 2018.

[10] Y. Ye, K. W. E. Cheng, and S. Chen, "A high step-up PWM DC-DC converter with coupled-inductor and resonant switched-capacitor," *IEEE Trans. Power Electron.*, vol. 32, no. 10, pp. 7739–7749, Oct. 2017.

[11] Y.-F. Wang, L.-K. Xue, C.-S. Wang, P. Wang, and W. Li, "Interleaved high-conversion-ratio bidirectional DC–DC converter for distributed energy-storage systems-circuit generation, analysis, and design," *IEEE Trans. Power Electron.*, vol. 31, no. 8, pp. 5547–5561, Aug. 2016.

[12] H. Heydari-doostabad and T. O'Donnell, "A wide-range high-voltage-gain bidirectional DC–DC converter for V2G and G2V hybrid EV charger," *IEEE Trans. Ind. Electron.*, vol. 69, no. 5, pp. 4718–4729, May 2022.

[13] Y. Xiao, Z. Zhang, M. A. E. Andersen, and B. Engelbrecht Thomsen, "Partial parallel dual active bridge converter with variable voltage gain for SOEC/SOFC system," in *Proc. IEEE Appl. Power Electron. Conf. Expo.*, 2019, pp. 1641–1646.

[14] H. Shi, K. Sun, H. Wu, and Y. Li, "A unified state-space modeling method for a phase-shift controlled bidirectional dual-active half-bridge converter," *IEEE Trans. Power Electron.*, vol. 35, no. 3, pp. 3254–3265, Mar. 2020.

[15] G. Xu, L. Li, X. Chen, Y. Liu, Y. Sun, and M. Su, "Optimized EPS control to achieve full load range ZVS with seamless transition for dual active bridge converters," *IEEE Trans. Ind. Electron.*, vol. 68, no. 9, pp. 8379–8390, Sep. 2021.

[16] S. Li, K. Xiangli, and K. M. Smedley, "A control map for a bidirectional PWM plus phase-shift-modulated push–pull DC–DC converter," *IEEE Trans. Ind. Electron.*, vol. 64, no. 11, pp. 8514–8524, Nov. 2017.

[17] N. Hou and Y. W. Li, "Overview and comparison of modulation and control strategies for a nonresonant single-phase dual-active-bridge DC–DC converter," *IEEE Trans. Power Electron.*, vol. 35, no. 3, pp. 3148–3172, Mar. 2020.

[18] H. Shi et al., "Minimum-backflow-power scheme of DAB-based solid-state transformer with extended-phase-shift control," *IEEE Trans. Ind. Appl.*, vol. 54, no. 4, pp. 3483–3496, Jul./Aug. 2018, doi: 10.1109/TIA.2018.2819120.

[19] Y.-E. Wu and Y.-T. Ke, "A novel bidirectional isolated DC–DC converter with high voltage gain and wide input voltage," *IEEE Trans. Power Electron.*, vol. 36, no. 7, pp. 7973–7985, Jul. 2021.

[20] H. Li et al., "Influences of device and circuit mismatches on paralleling silicon carbide MOSFETs," *IEEE Trans. Power Electron.*, vol. 31, no. 1, pp. 621–634, Jan. 2016.

[21] B. Zhao, Q. Song, J. Li, Y. Wang, and W. Liu, "Modular multilevel high-frequency-link DC transformer based on dual active phase-shift principle for medium-voltage DC power distribution application," *IEEE Trans. Power Electron.*, vol. 32, no. 3, pp. 1779–1791, Mar. 2017.

[22] M. Yaqoob, K. H. Loo, and Y. M. Lai, "Extension of soft-switching region of dual-active-bridge converter by a tunable resonant tank," *IEEE Trans. Power Electron.*, vol. 32, no. 12, pp. 9093–9104, Dec. 2017.

[23] Y.-F. Wang, B. Chen, Y. Hou, Z. Meng, and Y. Yang, "Analysis and design of a 1-MHz bidirectional multi-CLLC resonant DC–DC converter with GaN devices," *IEEE Trans. Ind. Electron.*, vol. 67, no. 2, pp. 1425–1434, Feb. 2020.

[24] M. Zhou, D. Shu, and H. Wang, "An H5-bridge-based laddered CLLC DCX with variable DC link for PEV charging applications," *IEEE Trans. Power Electron.*, vol. 37, no. 4, pp. 4249–4260, Apr. 2022.

[25] Y. Xiao, Z. Zhang, M. A. E. Andersen, and K. Sun, "Impact on ZVS operation by splitting inductance to both sides of transformer for 1-MHz GaN based DAB converter," *IEEE Trans. Power Electron.*, vol. 35, no. 11, pp. 11988–12002, Nov. 2020.

[26] Y.-F. Wang, L.-K. Xue, C.-S. Wang, P. Wang, and W. Li, "Interleaved high-conversion-ratio bidirectional DC–DC converter for distributed energy-storage systems—Circuit generation, analysis, and design," *IEEE Trans. Power Electron.*, vol. 31, no. 8, pp. 5547–5561, Aug. 2016.

Yiliang Li (Student Member, IEEE) was born in Heilongjiang Province, China, in 1996. He received the B.S. and M.S. degrees in electrical engineering in 2018 and 2020, respectively, from the Harbin Institute of Technology, Harbin, China, where he is currently working toward the Ph.D. degree in electrical engineering with the School of Electrical Engineering and Automation.

His current research interests include bidirectional dc–dc converter, electric vehicle charging, and energy storage system.

Yijie Wang (Senior Member, IEEE) was born in Heilongjiang Province, China, in 1982. He received the B.S., M.S., and Ph.D. degrees in electrical engineering from the Harbin Institute of Technology, Harbin, China, in 2005, 2007, and 2012, respectively.

From 2012 to 2014, he was a Lecturer with the Department of Electrical and Electronics Engineering, Harbin Institute of Technology. From 2014 to 2017, he was an Associate Professor with the Department of Electrical and Electronics Engineering, Harbin Institute of Technology. Since 2017, he has been a Professor with the Department of Electrical and Electronics Engineering, Harbin Institute of Technology. His interests include dc–dc converters, soft-switching power converters, power factor correction circuits, digital control electronic ballasts, LED lighting systems.

Dr. Wang is currently an Associate Editor for the IEEE TRANSACTIONS ON INDUSTRIAL ELECTRONICS, IEEE JOURNAL OF EMERGING AND SELECTED TOPICS IN POWER ELECTRONICS, IEEE ACCESS, *IET Power Electronics,* and *Journal of Power Electronics*.

Yueshi Guan (Senior Member, IEEE) was born in Heilongjiang Province, China, in 1990. He received the B.S., M.S., and Ph.D. degrees in electrical engineering from the Harbin Institute of Technology (HIT), Harbin, China, in 2013, 2015, and 2019, respectively.

Since 2019, he has been an Associate Professor with the Department of Electrical and Electronics Engineering, HIT. His research interests are in the areas of high frequency and very high frequency converters, single-stage ac–dc converter, and high-conversion-ratio converters.

Dianguo Xu (Fellow, IEEE) received the B.S. degree in control engineering from Harbin Engineering University, Harbin, China, in 1982 and the M.S. and Ph.D. degrees in electrical engineering from the Harbin Institute of Technology (HIT), Harbin, China, in 1984 and 1989, respectively.

In 1984, he joined the Department of Electrical Engineering, HIT, as an Assistant Professor. Since 1994, he has been a Professor with the Department of Electrical Engineering, HIT. He was the Dean of School of Electrical Engineering and Automation, HIT, from 2000 to 2010. He is currently the Vice President of HIT. His research interests include renewable energy generation technology, power quality mitigation, sensor less vector-controlled motor drives, high performance servo system. He authored or coauthored more than 600 technical papers.

Dr. Xu is currently an Associate Editor for the IEEE TRANSACTIONS ON INDUSTRIAL ELECTRONICS and the IEEE JOURNAL OF EMERGING AND SELECTED TOPICS IN POWER ELECTRONICS. He is currently a Chairman of IEEE Harbin Section.